Impurity confinement and transport in high confinement regimes without ELMs on DIII-D

B. A. Grierson,[1,*] K. H. Burrell,[2] R. M. Nazikian,[3] W. M. Solomon,[3] A. M. Garofalo,[2]
E. A. Belli,[2] G. M. Staebler,[2] M. E. Fenstermacher,[4] G. R. McKee,[5] T. E. Evans,[2]
D. M. Orlov,[6] S. P. Smith,[2] C. Chrobak,[2] C. Chrystal,[7] and the DIII-D team[2]

[1]*Princeton Plasma Physics Laboratory,*
Princeton University, Princeton, NJ 08543, USA
[2]*General Atomics, P.O. Box 85608,*
San Diego, CA 92186-5608, USA
[3]*Princeton Plasma Physics Laboratory,*
Princeton University, Princeton, NJ 08543, USA
[4]*Lawerence Livermore National Laboratory,*
P.O. Box 808, Livermore, CA 94550, USA
[5]*Department of Engineering Physics*
University of Wisconsin-Madison,
Madison, WI 53796, USA
[6]*Center for Energy Research, University of California San Diego,*
9500 Gilman Dr., La Jolla, CA 92093-0417, USA
[7]*University of California San Diego,*
9500 Gilman Dr., La Jolla, CA 92093-0417, USA

(Dated: January 29, 2015)

Abstract

Impurity transport in the DIII-D tokamak [J. L. Luxon, Nucl. Fusion **42**, 614 (2002)] is investigated in stationary high confinement (H-mode) regimes without edge localized modes (ELMs). In plasmas maintained by resonant magnetic perturbation (RMP) ELM-suppression and QH-mode the confinement time of fluorine (Z=9) is equivalent to that in ELMing discharges with 40 Hz ELMs. For selected discharges with impurity injection the impurity particle confinement time compared to the energy confinement time is in the range of $\tau_p/\tau_e \approx 2-3$. In QH-mode operation the impurity confinement time is shown to be smaller for intense, coherent magnetic and density fluctuations of the edge harmonic oscillation than weaker fluctuations. Transport coefficients are derived from the time evolution of the impurity density profile and compared to neoclassical and turbulent transport models NEO and TGLF. Neoclassical transport of fluorine is found to be small compared to the experimental values. In the ELMing and RMP ELM-suppressed plasma the impurity transport is affected by the presence of tearing modes. For radii larger than the mode radius the TGLF diffusion coefficient is smaller than the experimental value by a factor of 2-3, while the convective velocity is within error estimates. Low levels of diffusion are observed for radii smaller than the tearing mode radius. In the QH-mode plasma investigated, the TGLF diffusion coefficient higher inside of $\rho = 0.4$ and lower outside of 0.4 than the experiment, and the TGLF convective velocity is more negative by a factor of approximately 1.7.

PACS numbers: 52.25.vy, 52.25Fi, 52.35.Ra

*Electronic address: bgriers@pppl.gov

I. INTRODUCTION

Since the early experiments seeking to optimize the tokamak for magnetic confinement fusion, the importance of controlling impurities was realized [1]. Impurities in tokamaks can be intrinsic (first wall material, vessel components), self-generated (helium from fusion alpha particles that have thermalized) or introduced deliberately for impurity confinement and transport experiments (gas puffing, laser blow-off, pellets). In low confinement mode (L-mode) and improved L-mode (I-mode) plasmas, the particle confinement time of the main plasma particles and impurity ions (τ_p) is near or shorter than the energy confinement time (τ_e) and experimentally this is reflected in the significant fueling required to maintain the plasma density [2]. In the high confinement mode (H-mode) envisioned for a fusion reactor, particle confinement of the main plasma particles and impurities can be several times the energy confinement time ($\tau_p > \tau_e$), and can result in uncontrolled rises of the plasma density after the L→H transition. This uncontrolled density rise is typically called the "ELM-free" phase of the discharge, because the density rise has not been halted by the appearance of the first edge-localized mode (ELM). ELMs are periodic relaxations of the H-mode edge transport barrier that remove electrons, main-ions and impurities from the plasma core [3–7] (and reference therein) and is one mechanism by which stationary density can be maintained in the H-mode [8]. However, the ELM produces a large, transient heat flux to the tokamak divertor that can erode the plasma facing components and may be unacceptable in a fusion power reactor. The ELM acts both as an impurity exhaust mechanism, removing impurities from the plasma core, and also a trigger of impurity sources by physical sputtering and erosion, promoting influx of impurities [9]. An ideal ELM suppression solution replaces the ELM particle and impurity exhaust, without promoting plasma-material interactions that release impurities into the main chamber, possibly reducing the requirements on the exhaust rate.

Various strategies to mitigate ELMs and reduce the divertor heat flux are reviewed in Reference [10], including the resonant magnetic perturbation (RMP) ELM-suppression that eliminates ELMs, pellet pacing to increase the ELM frequency, and operational regimes with small rapid ELMs or naturally devoid of ELMs. Techniques used to completely eliminate ELMs currently used on DIII-D are RMP ELM-suppression [11] and operation in QH-mode [12]. Both of these techniques replace the ELM's particle exhaust with particle

transport resulting from magnetic fields either applied externally in RMP ELM-suppression, or self-generated as with the edge harmonic oscillation (EHO) in QH-mode, resulting in stationary plasma density. The challenge is to maintain energy confinement while providing sufficient particle exhaust. While the regulation of total plasma density is clearly obtained with these two techniques, the regulation of plasma impurity content when these mechanisms are applied requires deeper investigation. As an example, Fig. 1 displays the time history of an RMP ELM-suppressed discharge in which an influx of the first-wall material (carbon) occurs resulting in a higher impurity content than when ELMing. In ASDEX, it was found that high average Z_{eff} in QH-mode is dominated by light impurities and is due to increased impurity sources from counter-current neutral beam injection (NBI), as is commonly seen on other tokamaks [13].

Demonstration of stationary H-mode operation without ELMs in the presence of naturally occurring edge MHD has been obtained on other large tokamaks with studies performed on ASDEX, JET and EAST [14–16], and RMP ELM-mitigation on ASDEX [17], without reported increases in impurity content over ELMing H-mode; however no dedicated impurity transport studies have been done in these regimes.

In this work, we examine both the behavior of the intrinsic plasma impurities in DIII-D and impurities specifically introduced for confinement and transport studies. We find that although both the RMP ELM-suppressed and QH-mode plasmas can acquire relatively high concentrations of the intrinsic impurities when ELMs are suppressed, this is not due to an inherently long impurity confinement time, and these regimes can be operated at high plasma purity. Measurements of the time evolution of the concentration of introduced trace levels of fluorine indicate that the impurity confinement times are nearly equal in RMP ELM-suppressed, QH-mode and ELMing discharges with $f_{ELM} \approx 40$ Hz, and much less than in ELM-free discharges. Impurity transport equivalent to 40 Hz ELMs for low to medium Z impurities is consistent with meeting the requirements for helium exhaust in a fusion reactor, as demonstrated by Wade *et al.* in a series of seminal papers on helium exhaust [18–20], whereby 40 Hz ELMs on DIII-D produced $\tau_p^* \approx 8 - 11$, sufficient for meeting the requirements for helium exhaust in a reactor [$\tau_p* = \tau_p/(1-R)$ with R the effective recycling coefficient].

In the RMP ELM-suppressed and QH-mode conditions presented in this article, the relative impurity confinement time τ_p/τ_e is in the range of 2-3 (τ_e is the total energy con-

finement time). These values are comparable with ELMing impurity confinement times that obtain $\tau_p/\tau_e \leq 2$ for 40 Hz ELMs, but can be as large as $\tau_p/\tau_e \approx 4$ for lower frequency ELMs $f_{ELM} \leq 20$ Hz, also under stationary conditions. ITER demonstration discharges on DIII-D can display ELM frequencies ≤ 10 Hz [21] with density and impurity content that is poorly regulated due to the low ELM frequency. Similar operational requirements of increased ELM frequency are required for stationary operation in JET to avoid accumulation of tungsten [22]. This underscores the importance of rapid particle transport in high current scenarios.

In this paper we address the effectiveness of the RMP ELM-suppression and QH-mode to remove impurities from the plasma core. It has been demonstrated that the magnitude of the increased particle transport caused by the application of 3D field perturbations ("pumpout") scales with the applied field magnitude [23] and the impact extends into the plasma core [24]. The mechanism for RMP ELM-suppression may be due to formation of an island structure at the top of the H-mode pedestal [25], but the exact physical mechanism remains an active area of research. We find that the rate of particle transport across the edge particle barrier in QH-mode displays the same trend of increasing particle exhaust with the EHO amplitude and coherence, determined by trace fluorine injection decay times, and corroborated by measurements of the magnetic EHO intensity and beam emission spectroscopy (BES) density fluctuations. Modeling of the QH-mode indicates that a saturated kink-peeling mode is responsible for the fluctuations, and is currently being investigated with nonlinear MHD simulations [26].

In both RMP ELM-suppressed and QH-mode plasmas the transport coefficients of trace fluorine are determined experimentally in the plasma core (square-root of normalized toroidal flux $\rho_N < 0.8$) and are compared with neoclassical and turbulent transport models NEO [27] and TGLF [28, 29]. We find an under-prediction of the impurity diffusion with TGLF by approximately 2-3 in the outer regions of the plasma unaffected by tearing modes. In the outer regions of the plasma TLGF pinch velocities are in reasonable agreement with the experiment in the ELMing and RMP ELM-suppressed conditions. The QH-mode condition displays a radial diffusion profile higher inside of $\rho = 0.4$ and lower outside of 0.4 than the experiment, and the TGLF convective velocity is more negative by a factor of approximately 1.7.

II. ILLUSTRATION OF IMPURITY CONFINEMENT IN L-MODE, ELMING H-MODE AND ELM-FREE H-MODE

Impurity confinement in L-mode, ELMing H-mode and ELM-free H-mode can be clearly differentiated by the decay of impurity emission following a gas puff of a non-intrinsic, non-recycling impurity as displayed in Fig. 2, where short duration injection of chlorine (Z=17) gas was used to illustrate the impurity confinement time in these conditions. Figure 2(a) displays the time history of the plasma density and D_α photoemission for three discharges that all enter H-mode with high NBI power at 1000 ms, and then display different behavior after 2000 ms when the heating mixture is changed. The first discharge (black) falls out of H-mode and enters an L-mode phase. The time histories of two chlorine injections at 2200 and 3000 ms are displayed in Fig. 2(b) and for both injections the decay of the chlorine emission is rapid. The second injection occurs in steady conditions and has a decay constant $\tau_p \approx 72$ ms with a ratio $\tau_p/\tau_e \approx 0.9$. It can also be seen that there is little intrinsic nickel emission [Fig. 2(c)] and the fraction of radiated power [Fig. 2(d)] is modest and constant $P_{rad}/P_{aux} \approx 0.4$. The second discharge displayed in Fig. 2 remains in H-mode with low frequency ELMs at $f_{ELM} \approx 20$Hz. Here both chlorine injections occur in stationary conditions and the particle confinement time is $\tau_p \approx 480$ ms, much longer than L-mode, but by examining the density, intrinsic nickel levels and radiated power fraction we can see that the discharge has reached a transport equilibrium. In the second discharge (red), $\tau_p/\tau_e \approx 4.0$, or approximately four times the L-mode value. The final discharge (green) in Fig. 2 falls out of H-mode at 2300 ms and then enters an ELM-free H-mode at 3400 ms when the density is seen to rise continually. As the plasma enters ELM-free H-mode, the nickel and radiated power both begin to rise monotonically. A single chlorine injection was used at 4000 ms, and by examining the time history in Fig. 2(b) we can see that the plasma has integrated the chlorine gas puff and retained all particles. During the ELM-free phase of the third discharge in Fig. 2 the impurity particle confinement time is effectively infinite. Eventually, the ELM-free phase is terminated by radiative collapse when $P_{rad} > P_{aux}$.

In summary, we wish to operate in regimes with good energy confinement but poor particle confinement, especially of helium ash and higher-Z impurities that can lead to radiative collapse. While 20 Hz ELMs displayed in Fig. 2 are sufficient for density and impurity control, they may be marginal for helium control in a fusion reactor with the low

frequency unmitigated ELMs expected in ITER [30] because the particle confinement time may be relatively long compared to the energy confinement time.

III. IMPURITY CONFINEMENT IN ELMING, RMP ELM-SUPPRESSED AND QH-MODE

In this section, we present the measurements of fluorine (Z=9) emission following short gas puffs in ELMing, RMP ELM-suppressed and QH-mode plasmas using a technique previously reported in Reference [31]. Discharges with $n = 3$ RMPs applied to suppress ELMs on DIII-D are typically executed with edge electron collisionality $\nu_* \leq 0.30$, $\beta_N \geq 1.4$ and q_{95} between 3.1-3.6 [11] to obtain ELM suppression. The discharges are begun by entering an ELMing H-mode with co-I_p NBI, establishing quasi-steady conditions, and then applying the RMP to suppress the ELMs. These shots are characterized by large sawteeth due to the low q_{95} and commonly have $m/n = 4/3$ and $3/2$ tearing modes, where m is the poloidal mode number and n is the toroidal mode number. QH-modes in this study are executed with early NBI heating in the direction counter to the plasma current, and enter a rapidly counter-I_p rotation state for the first 1-1.5 seconds of the shot to enter the QH-mode phase, and then subsequently the density may be raised or balance of injected torque modified for study.

After a short (10 ms) gas puff, fluorine enters the plasma and propagates all the way to the magnetic axis. Fluorine emission peaks at the magnetic axis within approximately 50-80 ms in the QH-mode and decays afterwards. The duration of the rise phase is longer in the RMP discharges in the presence of tearing modes and sawtooth precursor oscillations than in the QH-modes, which do not have measurable core MHD. Beyond the peak of the fluorine emission the signal possesses an exponential decay character and defines the particle confinement time τ_p. Formally, the particle confinement time is the decay constant of the radial eigenmode that possesses the longest decay time. Once the radial profile of this eigenmode is established, the impurity density profile decays self-similarly. The confinement time is set by the rate of transport across the edge barrier because there is no core source of fluorine. In the QH-mode, the signals decay exponentially with a time constant that is independent of radius because the radial eigenmode is established rapidly. In plasmas with core tearing modes and sawtooth precursor oscillations, the radial eigenfunction is

established rapidly for plasma radii larger than the MHD, and more slowly for radii inside of the core MHD. Therefore, in order to compare the decay constants between plasmas without and with core MHD, we report the impurity confinement time at large radius.

The first condition we investigate is an ELMing plasma for attempted RMP ELM-suppression with large ELMs occurring at nearly constant frequency of 40.5 Hz between 1800-2200 ms. This discharge, 156823, is executed with $I_p = 1.42$ MA, $B_T = -1.97$ T, line-averaged density $\langle n_e \rangle \approx 3.4 \times 10^{19}$ m^{-3}, $\beta_N = 1.73$, $q_{95} = 3.98$, and 5.82 MW of NBI. Fluorine is injected and monitored with charge-exchange recombination (CER) spectroscopy and is seen to have an exponential decay character after its peak during constant ELM frequency, seen in Fig. 3. During 40 Hz ELMs the decay constant is $\tau_p \approx 335$ ms and confinement ratio is $\tau_p/\tau_e \approx 2.2$. After 2200 ms the ELM frequency increases and the confinement time becomes shorter during 65 Hz ELMs. For a given ELM amplitude (exhaust of density across the ELM), the particle loss due to the ELM is inversely proportional to the ELM frequency [7].

The second condition presented is during RMP ELM-suppression. Discharge 154858, displayed in Fig. 1, is executed with $I_p = 1.54$ MA, $B_T = -1.92$ T, $\langle n_e \rangle \approx 3.0 \times 10^{19}$ m^{-3}, $\nu_* \approx 0.1 - 0.2$, $\beta_N \approx 1.8 - 1.9$, $q_{95} = 3.55$ and 5.89 MW of NBI. 2.8 kA of current is initially applied to the DIII-D in-vessel coils (I-coils) with the current subsequently increasing stepwise, resulting in reduction of the plasma density and suppression of ELMs. Shortly after the ELMs are suppressed fluorine is injected, and decays with time constant of $\tau_p \approx 317$ ms as seen in Fig. 4. Although Z_{eff} from the intrinsic carbon begins to rise over this time period (n_C increases from 0.1 to 0.2 $\times 10^{19}$ m^{-3} at $\rho = 0.74$), seen in Fig. 1, the non-intrinsic impurity fluorine is rapidly expelled. While the carbon density appears to rise in a manner similar to the ELM-free discharge in Fig. 2, this must be due to an increased source of carbon, and not an inherently long impurity confinement time. The increased source can be due to changes in the parallel transport to the divertor plates or increased beam ion losses due to the 3D field perturbation. In this plasma, the energy confinement time is higher than the ELMing plasma displayed in Fig. 3 due to the higher current, and this results in a ratio of particle confinement to energy confinement of $\tau_p/\tau_e \approx 1.8$.

In QH-mode plasmas, the rate of electron particle exhaust is proportional to the amplitude of the EHO MHD oscillation [32], and here we present two different QH-mode discharges displayed in Figs 5 and 6 that are operated the same plasma conditions, with one difference;

discharge 153302 has 6 kA of toroidal mode number $n = 3$ non-resonant external field coil current applied to the DIII-D "C-coils". Discharges 153291 and 153302 are executed with $I_p = -1.21$ MA, $B_T = -1.93$ T, $\langle n_e \rangle = 2.6 \times 10^{19}$ m^{-3}, $\nu_* \approx 0.1 - 0.2$, $\beta_N \approx 1.8 - 1.9$, $q_{95} = 4.78$ and 5.75 MW of NBI. In discharge 153291 (Fig. 5), the edge harmonic oscillation is coherent and dominated by $n = 3$, with $n = 2$ and $n = 1$ sub-harmonics also visible. Application of the C-coils in 153302 affects the EHO character, making the coherent magnetic fluctuations seen in Fig. 5(b) become less coherent, but still of finite amplitude with a more "broadband" character, seen in Fig. 6(b). Due to the lower intensity of the EHO when it presents a broadband magnetic signature, the particle exhaust is less rapid. This reduced particle transport can be seen by comparing Fig. 5(c) and Fig. 6(c) where the impurity confinement time is $\tau_p \approx 327$ ms with coherent QH-mode operation, and a longer confinement time of $\tau_p \approx 405$ ms when the EHO is broadband. Magnetic measurements are dependent on the proximity of the plasma to the pickup coils and are not a local measurement. However, using beam emission spectroscopy to deduce the local density fluctuations caused by the EHO, the local fluctuation intensity can be compared between coherent and broadband EHO. Figure 7 displays the beam emission intensity at $\rho = 0.96$ for coherent and broadband EHO, demonstrating that the coherent EHO has the largest low frequency fluctuation intensity, and that the broadband EHO possesses 80% of the intensity of the coherent EHO when integrated over the frequency domain. The coherent EHO produces particle transport equivalent to 40 Hz ELMs seen in Fig. 3, with a similar ratio of particle to energy confinement time $\tau_p/\tau_e \approx 2.4$, while the broadband EHO presents a somewhat higher ratio of $\tau_p/\tau_e \approx 3.0$. It is noteworthy that the ratio of particle confinement time to energy confinement time can be minimized when operating QH-mode at low injected torque [31]. In both cases, we clearly see that the impurity confinement time is less than that for 20 Hz ELMs seen in Fig. 2, and much less than standard ELM-free operation.

In summary, we have shown that both RMP ELM-suppressed and QH-mode discharges accomplish impurity particle transport equivalent to 40 Hz ELMs in DIII-D, with $\tau_p/\tau_e \approx 2$ sufficient for impurity control, and much less than standard ELM-free impurity confinement.

IV. IMPURITY TRANSPORT COEFFICIENTS

In the previous sections, we have investigated the global particle exhaust in ELMing H-mode plasmas and plasmas designed to eliminate ELMs. Both techniques of RMP ELM-suppression and QH-mode achieve rapid impurity exhaust equivalent to 40 Hz ELMs. In this section, we investigate the core impurity transport in these two conditions. First, we examine the plasma profiles and compute the expected turbulent mode activity. Stiff turbulent fluxes are extremely sensitive to the driving gradients. In order to compare experimental transport coefficients to model-based coefficients, we use TGYRO [33] to obtain the flux-matching profiles with NEO [27] and TGLF [28, 29] to match the power balance fluxes obtained from TRANSP [34] and NUBEAM [35]. Having obtained flux-matching profiles, we determine the neoclassical and turbulent D and V predicted by NEO and TGLF. These transport coefficients are then compared to the coefficients derived from experimental data.

A. Experimental and flux-matching profiles

Three discharge conditions are investigated represented by plasma profiles presented in Fig. 8. The ELMing, RMP ELM-suppressed and QH-mode discharge conditions are the same as reported in Sec. III, except that this QH-mode has higher NBI torque and toroidal rotation. The ELMing and RMP ELM-suppressed discharges have core tearing mode activity diagnosed with magnetic measurements and electron cyclotron emission (ECE) fluctuation analysis. In the ELMing plasma an $n = 2$ tearing mode is growing near $\rho = [0.35 - 0.5]$ and an $n = 3$ tearing mode is growing near $\rho \approx 0.2$. One feature of note is the relatively flat spot in the toroidal rotation profile for the RMP ELM-suppressed plasma between $\rho_N \approx 0.2 - 0.45$ near the 4/3 rational surface. Magnetic measurements indicate that there is a saturated 4/3 tearing mode, and MSE-constrained q-profile and ECE cross-phase analysis indicates that the mode is located near $\rho \approx 0.38$. Later in this section we will see the impact these modes have on impurity transport. No core tearing modes are observed for the QH-mode.

Linear turbulence growth rates calculated by TGLF for these three conditions are displayed in Fig. 9, where we report the growth rates γ for $k_\theta \rho_S \leq 1.0$ where ion temperature gradient (ITG) and trapped electron modes (TEM) typically dominate the turbulence spectrum. Here, the values of γ_e and γ_i reported are the growth rates where the quantity

$\gamma/(k_\theta \rho_S)^2$ is maximized, as a mixing-length estimate for identifying modes that will most strongly contribute to transport. Also included in the figure is the $E \times B$ shearing rate $\gamma_{E\times B} = -(r/q)\partial\omega_0/\partial r$ for reference, where r is the minor radius, q is the safety factor and ω_0 is the $E \times B$ rotation frequency defined as $-c\partial\Phi/\partial\psi$. In the ELMing plasma linear growth rates are above $\gamma_{E\times B}$ for $\rho > 0.5$ and we expect that low-k turbulence will be minimal inside of $\rho = 0.5$. In the RMP ELM-suppressed plasma, the outer region of the radial profile is dominated by $\gamma_i > \gamma_{E\times B}$. Here we expect ion modes to promote inward particle convection, whereas inside of $\rho_N \approx 0.4$ electron modes dominate where stronger outward particle transport is expected. The location of peak electron growth rate is also coincident with the minimum in $\gamma_{E\times B}$ at the 4/3 surface. For the QH-mode discharge, the turbulence is dominated by low-k ion modes across most of the radial domain, and we expect an inward particle convection driven by ITG modes across the profile.

Profiles of n_e, T_e and T_i that are consistent with the power flows obtained with TRANSP and NUBEAM are displayed for the ELMing, RMP ELM-suppressed and QH-mode discharges in Figs 10, 11, 12, respectively, produced by the TGYRO transport solver. These profiles are obtained by adjusting the local gradients $a/L_{ne}, a/L_{Te}$ and a/L_{Ti} such that Γ_e, Q_e and Q_i from NEO+TGLF match the transport fluxes, forming new profiles. In the ELMing plasma (Fig. 10), the profiles are in reasonably good agreement with the experimental profiles. In the deep core the solution has difficulty converging for $\rho = 0.28$, and produces a local change in a/L_{ne} that oscillates in time. For this reason, later in this article we will neglect this region when reporting impurity transport coefficients. Consistent with linear stability seen in Fig. 9(a), a steep gradient develops in the TGYRO T_i profile near $\rho = 0.4$. With the high $\gamma_{E\times B}/\gamma_i$, the ion thermal transport is neoclassical in this region. For the RMP ELM-suppression discharge (Fig. 11), the flux-matching profiles are in good agreement with the experimental profiles. With reduced rotation due to the presence of the saturated 4/3 tearing mode there is significant ion turbulence flux and the the ion thermal transport has a higher turbulence contribution than the ELMing plasma in Fig. 10. The agreement of the QH-mode profiles (Fig. 12) is less satisfactory than the ELMing and RMP ELM-suppressed plasmas, with density predictions flatter, T_e lower and T_i higher than the experimental profiles. Nevertheless, in order to make progress we will use flux-matching profiles moving forward and note that the reduced peaking of n_e in the QH-mode discharge will reduce the NEO neoclassical inward convection near the magnetic axis. Using the ex-

perimental a/L_{Ti} at $\rho = 0.8$, for example, results is little transport flux and a/L_{Ti} must be raised from 1.4 to 2.5 in order for TGLF to remove the experimental level of energy through the ion channel.

B. Impurity transport coefficients

Radial particle transport is commonly cast in the pinch-diffusion formulation, with transport coefficients of particle diffusion D and convective velocity V, given in Eq. (1)

$$\begin{aligned} \frac{\partial n}{\partial t} + \nabla \cdot \Gamma &= S \\ \Gamma &= -D\nabla n + Vn \quad . \end{aligned} \tag{1}$$

Neoclassical theory derives D and V from collisional mechanisms, whereas turbulent particle transport produces D and V dependent on turbulent fluctuations driven by gradients in the background profiles. Reviews of these topics are given in References [36] and [37] where it can be seen that there are many separate mechanisms embodied in the effective D and V in the present formulation. Experimentally, D and V can be determined by recording the spatio-temporal evolution of an impurity density following laser blow-off or a short gas puff. In order to extract both D and V, one must resolve the rise of the impurity density, because well beyond the peak of the impurity density time derivatives are small, $\Gamma \approx 0$, and only the ratio V/D "peaking factor" can be determined.

In this article, we choose to use the impurity transport simulation code STRAHL [38, 39] to determine D and V. For our STRAHL simulations we use time-independent transport coefficients. Initial guesses for $D(\rho), V(\rho)$ are formed as radial profiles from the magnetic axis out into the scrape-off layer, and then iterated upon until the modeled $n_z(r,t)$ matches the observed $n_z(r,t)$. Here $\chi^2 = (n_Z^{exp} - n_Z^{STRAHL})^2/\sigma^2$ for all measurement points, with σ being the uncertainty in the impurity density. By using the Levenberg-Marquart minimization with MPFIT [40] reducing χ^2, D and V consistent with the observed impurity density spatio-temporal evolution can be determined with uncertainty estimates in a manner similar to References [41] and [42]. The results of this procedure for ELMing, RMP ELM-suppressed and QH-mode discharges are illustrated in Figs 13, 14 and 15, where one can see that the STRAHL modeling matches the experimental density evolution. For the simulations reported in this article, fluorine is constrained to have a recycling coefficient of $R = 0.0$

and the gas puff waveform used is a "top-hat" function, with start time, stop time and magnitude of gas flow (particles/s) able to be adjusted around their experimental values in the minimization procedure. Therefore we will only report transport coefficients inside of the outer-most radius due to the uncertainties in the particle source.

Time evolution and STRAHL modeling for the ELMing and RMP ELM-suppressed discharges that possess core tearing modes are displayed in Figs 13 and 14. By examining the time evolution for both of these discharges a few characteristics can be easily seen. For radii larger than $\rho \approx 0.4$ [Fig. 13(a,b) and Fig. 14(a-d)], the rise of fluorine density is rapid, occurring in a few measurement points obtained at 2.5 ms time resolution. Inside of $\rho \approx 0.4$ the rise of fluorine is much slower. This implies a change change in transport near $\rho \approx 0.4$ from fast inward (relatively higher D and/or high negative V for $\rho > 0.4$) to much slower (relatively lower D and V for $\rho < 0.4$). It is noteworthy that $\rho \approx 0.4$ is the radius of tearing mode activity in these discharges, and will be discussed in later sections. In the QH-mode discharge presented in Fig. 15, during the first few measurements the fluorine density increases rapidly across the entire radius. The rapid rise of fluorine density observed is approaching the time resolution of the measurements in these conditions, and increases the uncertainty in the derived transport coefficients. We note that the time evolution of measurements near the magnetic axis [Fig. 15(f,g)] displays a systematically higher and lower fluorine density, respectively, in the STRAHL modeling compared to the measurements, but remain within error bars. The χ^2 minimization with MPFIT has compromised between the weighting of these two channels when deducing the transport coefficients.

Transport coefficients for the ELMing plasma are presented in Fig. 16 with the transport coefficients from NEO and TGLF. Diffusion outside of $\rho = 0.4$ is large, being approximately a factor of 2-3 above the TGLF diffusion, with negligible neoclassical particle diffusion. The convection velocity for radii outside of $\rho = 0.4$ is in reasonable agreement with TGLF where the turbulence is predicted to be dominated by ion modes. For radii inside of $\rho = 0.4$, the measured diffusion is dramatically reduced. Due to the strong ion temperature gradient, the neoclassical convection becomes slightly positive, which acts to screen impurities [43]. However, the observed positive convection velocity just inside of $\rho = 0.4$ is larger than either the TGLF or NEO models. These features in the transport coefficients promote rapid inward transport from the plasma edge in to $\rho \approx 0.4$, but then reduce the rate of impurity uptake towards the magnetic axis. Once fluorine reaches the magnetic axis, small levels of

diffusion inhibit cross-field radial transport. The peaking factor (V/D) indicates that the impurity density will possess a positive gradient near $\rho = 0.4$, and indeed this is observed in the fluorine and carbon density profiles.

In Fig. 17 we present the experimental transport coefficients for the RMP ELM-suppressed condition, alongside the transport coefficients from NEO+TGLF. Experimentally, the transport coefficients outside of $\rho \approx 0.4$ are large in magnitude with $D \approx 5 - 10$ m^2/s, and V negative, but with a large uncertainty due to the rapid influx and few data points during the rise of the impurity density. These coefficients promote rapid transport from the edge to $\rho = 0.4$, as expected from ion turbulence seen in the linear growth rate spectrum in Fig. 9(b). Inside of $\rho \approx 0.4$ diffusion is strongly reduced and the convective velocity is slightly positive, where both of these features in the transport coefficients inhibit impurities from entering or exiting the deep core. Indeed the time history of the inner-most measurement displays a slow rise and fall of the fluorine density, consistent with the low level of diffusion. Model-based transport coefficients are overplotted in Fig. 17 from NEO and TGLF individually, and combined. For most of the radius, the neoclassical D and V are small compared to the experimental values. However nearer to the magnetic axis the neoclassical convective velocity is within the experimental uncertainty. This deep core region ($\rho < 0.2$) is where the ion thermal transport becomes neoclassical, and there is little turbulent ion energy flux. The TGLF diffusion coefficient is of the proper order of magnitude to be relevant, but the radial profile is poorly matched. In the outer regions of the plasma, the particle diffusion coefficient is under-predicted, while in the inner regions of the plasma the diffusion is over-predicted. The convective velocity for $\rho \geq 0.4$ is in agreement with TGLF, however the error bar is large due to the relatively few experimental measurements during the rapid rise of the fluorine density. The peaking factor obtained from TGLF and NEO+TGLF is quite flat across the radius, but does display a trend towards zero in the radial region where electron modes are active, in accordance with electron dominated transport driving stronger outward particle flux than ion modes.

In the comparison of the ELMing and RMP ELM-suppressed discharges we have neglected the presence of a 4/3 tearing mode at $\rho \approx 0.4$. It is clear that the location of the NTM is a dividing line between high and lower particle diffusion, and the radial region in which the particle convective velocity changes sign. We posit that the transport coefficients inside of the radii where NTMs exist are strongly affected by the occurrence of the modes, and should

not be directly compared to turbulent or neoclassical transport coefficients that neglect magnetic islands. Nevertheless, we take this opportunity to state the need for transport models that incorporate MHD phenomena, as advanced, high performance scenarios are typically accompanied by saturated tearing modes that can significantly affect all transport channels (particle, energy and momentum) and the impurity dynamics [44, 45]. In the RMP ELM-suppressed example, the presence of the mode strongly modifies the local $E \times B$ shearing rate with little apparent impact on n_e, T_e and T_i profiles.

In the QH-mode discharge, with profiles displayed in Fig. 8 and growth rates in Fig. 9(c), there is no core MHD from sawteeth or tearing modes and we expect the transport models to more accurately capture the transport coefficients. Due to the dominance of low-k ion modes, we expect a strong inward convection, and indeed this is what is observed. Figure 18 displays the transport coefficients extracted from STRAHL modeling, as well as the coefficients from neoclassical and turbulent transport. For the QH-mode plasma, a small amount local radial profile variation for D and V is required to match the time evolution of the fluorine density, resulting in smooth transport coefficients without sharp features or changes in the sign of V. Combining the diffusion and convective velocity profiles produces the peaking factor V/D, which indicates the shape of the density profile. A negative V/D means that the profile will maintain a peaked character with positive a/L_n, and a flat profile from strong diffusion relative to convection is associated with $|V/D| < 1$. Neoclassical transport coefficients are well below the observed D and V, and the neoclassical peaking factor indicates that the fluorine density should be very peaked. NEO produces a negative V/D across the entire profile driven by the peaked density profile seen in Fig. 8. $V/D < 0$ is a common concern for regimes that operate with neoclassical impurity transport and peaked profiles due to impurity accumulation. TGLF D and V are qualitatively consistent with the observed coefficients, with a diffusion and pinch velocity that increase in magnitude with minor radius. However, the diffusion is under-predicted by approximately a factor of two at large radius.

In a predictive simulation based on neoclassical and turbulent transport, the combined NEO+TGLF coefficients in Fig. 17 can be used directly to determine the evolution of the fluorine density. In Fig. 19 we bring the model to the data and simulate the fluorine density evolution, once again matching the outer-most measurement by design. During the density rise in Fig. 19(c,d) we see that the simulation transports the particles less rapidly than observed experimentally, and this is a result of the under-prediction of the particle diffusion

coefficient in Fig. 14. For channels inside of $\rho \approx 0.38$ the simulated particle density peaks earlier and decays more rapidly than in the experiment. The impact of the tearing mode on the impurity transport can be interpreted as beneficial, in that the experimental influx is less rapid and does not obtain quite as peaked of a density profile. However this benefit comes at the cost of the longer on-axis impurity confinement times. In this discharge, the fluorine density remains peaked until the occurrence of the first sawtooth crash that appears at 3300 ms, coming 800 ms after the gas puff, at which point the central fluorine density is flattened.

V. DISCUSSION AND CONCLUSIONS

In this work we have shown that ELM control techniques, RMP ELM-suppression and QH-mode, have impurity transport across the edge barrier comparable to ELMing plasmas with ELM frequencies near 40 Hz. These exhaust rates are much faster than the ITER baseline demonstration discharges on DIII-D and the unmitigated large, low frequency ELMs seen in JET high current operation [22] and unmitigated low frequency ELMs expected in ITER [30]. This exhaust rate also compares favorably with previous work on helium transport, indicating that regimes without ELMs such as RMP ELM-suppression and QH-mode may successfully replace ELMs for removal of helium ash in a fusion reactor. Further, suppression of the ELM, which removes a dominant source of impurities, while maintaining impurity exhaust, may tip the balance towards high purity operation if the sputtering yield can be kept lower than that produced by ELMs by coupling detached divertor operation to the regimes described in this article.

Core transport coefficients in these regimes display features expected from turbulent transport in regions without MHD, however the presence of MHD strongly affect the impurity influx and retainment, and is an area that requires dedicated study. In regions of the plasma where the calculated turbulent spectrum is dominated by modes in the ion drift direction by TGLF, the observed and calculated inward impurity convection is rapid, as expected from quasi-linear considerations [37]. Future research efforts will extend these results to higher-Z impurities, and determine if the ELM-effective scaling is independent of impurity charge.

VI. ACKNOWLEDGMENTS

This material is based upon work supported by the U.S. Department of Energy, Office of Science, Office of Fusion Energy Sciences, using the DIII-D National Fusion Facility, a DOE Office of Science user facility, under Awards DE-AC02-09CH11466, DE-FC02-04ER54698, DE-AC52-07NA27344, DE-FG02-89ER53296, and DE-FG02-08ER54999. DIII-D data shown in this paper can be obtained in digital format by following the links at https://fusion.gat.com/global/D3D_DMP. B.A. Grierson acknowledges valuable discussion with R. Dux and N. Howard.

[1] K. Ida, R. Fonck, S. Sesnic, R. Hulse, and B. LeBlanc, Phys. Rev. Lett. **58**, 116 (1987).

[2] N. T. Howard, M. Greenwald, and J. E. Rice, Rev. Sci. Instrum. **82**, 033512 (2011).

[3] M. Yamada, Fusion Eng. and Design **15**, 325 (1991).

[4] ITER Physics Expert Group on Divertor, ITER Physics Expert Group on Divertor Modelling and Database and ITER Physics Basis Editors, Nucl. Fusion **39**, 2391 (1999).

[5] H. Zohm, Nucl. Fusion **39**, 2391 (1999).

[6] A. Loarte, G. Saibene, R. Sartori, D. Campbell, M. Becoulet, L. Horton, T. Eich, A. Herrmann, G. Matthews, N. Asakura, A. Chankin, A. Leonard, G. Porter, G. Federici, G. Janeschitz, M. Shimada and M. Sugihara, Plasma Phys. Controlled Fusion **45**, 1549 (2003).

[7] M. R. Wade, K. H. Burrell, A. W. Leonard, T. H. Osborne, and P. B. Snyder, Phys. Rev. Lett. **94**, 225001 (2005).

[8] G. D. Porter, T. A. Casper, and J. M. Moller, Phys. Plasmas **8**, 4140 (2001).

[9] R. Dux, A. Janzer, T. Pütterich, and ASDEX Upgrade Team, Nucl. Fusion **51**, 053002 (2011).

[10] P. T. Lang, A. Loarte, G. Saibene, L. R. Baylor, M. Becoulet, M. Cavinato, S. Clement-Lorenzo, E. Daly, T. E. Evans, M. E. Fenstermacher, Y. Gribov, L. D. Horton, C. Lowry, Y. Martin, O. Neubauer, N. Oyama, M. J. Schaffer, D. Stork, W. Suttrop, P. Thomas, M. Tran, H. R. Wilson, A. Kavin, and O. Schmitz, Nucl. Fusion **53**, 043004 (2013).

[11] Todd E. Evans, Richard A. Moyer, Keith H. Burrell, Max E. Fenstermacher, Ilon Joseph, Anthony W. Leonard, Thomas H. Osborne, Gary D. Porter, Michael J. Schaffer, Philip B. Snyder, Paul R. Thomas, Jonathan G. Watkins, and William P. West, Nat. Phys. **2**, 419 (2006).

[12] K. H. Burrell, A. M. Garofalo, W. M. Solomon, M. E. Fenstermacher, D. M. Orlov, T. H. Osborne, J.-K. Park, and P. B. Snyder, Nucl. Fusion **53**, 073038 (2013).

[13] W. Suttrop, G. D. Conway, L. Fattorini, L. D. Horton, T. Kurki-Suonio, C. F. Maggi, 2003)M. Maraschek, H. Meister, R. Neu, Th Pütterich, M. Reich, A. C. C. Sips, and the ASDEX Upgrade Team, Plasma Phys. Controlled Fusion **46**, A151 (2004).

[14] W. Suttrop, V. Hynönen, T. Kurki-Suonio, P. T. Lang, M. Maraschek, R. Neu, A. Stbler, G. D. Conway, S. Hacquin, M. Kempenaars, P. J. Lomas, M. F. F. Nave, R. A. Pitts, K.-D. Zastrow, the ASDEX Upgrade team and contributors to the JET-EFDA workprogramme,

Nucl. Fusion **45**, 721 (2005).

[15] E. R. Solano, P. J. Lomas, B. Alper, G. S. Xu, Y. Andrew, G. Arnoux, A. Boboc, L. Barrera, P. Belo, M. N. A. Beurskens, M. Brix, K. Crombe, E. de la Luna, S. Devaux, T. Eich, S. Gerasimov, C. Giroud, D. Harting, D. Howell, A. Huber, G. Kocsis, A. Korotkov, A. Lopez-Fraguas, M. F. F. Nave, E. Rachlew, F. Rimini, S. Saarelma, A. Sirinelli, S. D. Pinches, H. Thomsen, L. Zabeo, and D. Zarzoso, Phys. Rev. Lett. **104**, 185003 (2010).

[16] H. Q. Wang, G. S. Xu, B. N. Wan, S. Y. Ding, H. Y. Guo, L. M. Shao, S. C. Liu, X. Q. Xu, E. Wang, N. Yan, V. Naulin, A. H. Nielsen, J. Juul Rasmussen, J. Candy, R. Bravenec, Y. W. Sun, T. H. Shi, Y. F. Liang, R. Chen, W. Zhang, L. Wang, L. Chen, N. Zhao, Y. L. Li, Y. L. Liu, G. H. Hu, and X. Z. Gong, Phys. Rev. Lett.. **112**, 185004 (2014).

[17] W. Suttrop, T. Eich, J. C. Fuchs, S. Günter, A. Janzer, A. Herrmann, A. Kallenbach, P. T. Lang, T. Lunt, M. Maraschek, R. M. McDermott, A. Mlynek, T. Pütterich, M. Rott, T. Vierle, E. Wolfrum, Q. Yu, I. Zammuto, H. Zohm and ASDEX Upgrade Team, Phys. Rev. Lett.. **106**, 225004 (2011).

[18] M. R. Wade, D. L. Hillis, J. T. Hogan, R. Maingi, M. M. Menon, M. A. Mahdavi, W. P. West, K. H. Burrell, P. Gohil, R. J. Groebner, R. M. Hong, D. H. Kellman, J. C. Phillips, R. P. Seraydarian, the DIII–D Team and D. F. Finkenthal, Phys. Plasmas **2**, 2357 (1995)

[19] M. R. Wade, T. C. Luce, and C. C. Petty, Phys. Rev. Lett. **79**, 419 (1997).

[20] M. R. Wade, W. A. Houlberg, L. R. Baylor, W. P. West, and D. R. Baker, J. Nucl. Mater. **290**, 773 (2001).

[21] E. J. Doyle, J. C. DeBoo, J. R. Ferron, G. L. Jackson, T. C. Luce, M. Murakami, T. H. Osborne, J.-M. Park, P. A. Politzer, H. Reimerdes, R. V. Budny, T. A. Casper, C. D. Challis, R.!J. Groebner, C.!T. Holcomb, A. W. Hyatt, R.!J. La Haye, G. R. McKee, T. W. Petrie, C. C. Petty, T. L. Rhodes, M. W. Shafer, P. B. Snyder, E. J. Strait, M. R. Wade, G. Wang, W. P. West, and L. Zeng, Nucl. Fusion **50**, 075005 (2010).

[22] F. Romanelli and J.-E. Contributors, Nucl. Fusion **53**, 104002 (2013).

[23] T. E. Evans, M. E. Fenstermacher, R. A. Moyer, T. H. Osborne, J. G. Watkins, P. Gohil, I. Joseph, M. J. Schaffer, L. R. Baylor, M. Bcoulet, J. A. Boedo, K. H. Burrell, J. S. deGrassie, K. H. Finken, T. Jernigan, M. W. Jakubowski, C. J. Lasnier, M. Lehnen, A. W. Leonard, J. Lönnroth, E. Nardon, V. Parail, O. Schmitz, B. Unterberg, and W. P. West, Nucl. Fusion **48**, 024002 (2008).

[24] S. Mordijck, E. J. Doyle, G. R. McKee, R. A. Moyer, T. L. Rhodes, L. Zeng, N. Commaux, M. E. Fenstermacher, K. W. Gentle, H. Reimerdes, O. Schmitz, W. M. Solomon, G. M. Staebler, and G. Wang, Phys. Plasmas **19**, 056503 (2012).

[25] M. R. Wade, R. Nazikian, J. S. deGrassie, T. E. Evans, N. M. Ferraro, R. A. Moyer, D. M. Orlov, R. J. Buttery, M. E. Fenstermacher, A. M. Garofalo, M. J. Lanctot, G. R. McKee, T. H. Osborne, M. W. Shafer, W. M. Solomon, P. B. Snyder, W. Suttrop, A. Wingen, E. A. Unterberg and L. Zeng, Nucl. Fusion **55**, 023002 (2015).

[26] F. Liu, G. T. A. Huijsmans, A. Loarte, A. M. Garofalo, W. M. Solomon, and M. Hoelzl, "Nonlinear MHD Simulations of QH-mode Plasmas in DIII-D," in *Proc. of 41st EPS Conf. on Plasma Physics* (Berlin, Germany) 2014.

[27] E. A. Belli and J. Candy, Plasma Phys. Controlled Fusion **50**, 095010 (2008).

[28] G. M. Staebler, J. E. Kinsey, and R. E. Waltz, Phys. Plasmas **12**, 102508 (2005).

[29] G. M. Staebler, J. E. Kinsey, and R. E. Waltz, Phys. Plasmas **14**, 155909 (2007).

[30] A. Loarte, G. Huijsmans, S. Futatani, L. R. Baylor, T. E. Evans, D. M. Orlov, O. Schmitz, M. Becoulet, P. Cahyna, Y. Gribov, A. Kavin, A. Sashala Naik, D. J. Campbell, T. Casper, E. Daly, H. Frerichs, A. Kischner, R. Laengner, S. Lisgo, R. A. Pitts, G. Saibene, and A. Wingen, Nucl. Fusion **54**, 033007 (2014).

[31] B. A. Grierson, K. H. Burrell, A. M. Garofalo, W. M. Solomon, A. Diallo, and M. O'Mullane, Nucl. Fusion **54**, 114011 (2014).

[32] K. H. Burrell, M. E. Austin, D. P. Brennan, J. C. DeBoo, E. J. Doyle, C. Fenzi, C. Fuchs, P. Gohil, C. M. Greenfield, R. J. Groebner, L. L. Lao, T. C. Luce, M. A. Makowski, G. R. McKee, R. A. Moyer, C. C. Petty, M. Porkolab, C. L. Rettig, T. L. Rhodes, J. C. Rost, B. W. Stallard, E. J. Strait, E. J. Synakowski, M. R. Wade, J. G. Watkins, and W. P. West, Phys. Plasmas **8**, 2153 (2001).

[33] J. Candy, C. Holland, R. E. Waltz, M. R. Fahey, and E. Belli, Phys. Plasmas **16**, 060704 (2009).

[34] R. J. Hawryluk, "An Empirical Approach," *Physics of Plasmas Close to Thermonuclear Conditions*, B. Coppi, Editor, published for Commission of the European Communities, International School of Plasma Physics (Pergamon Press, 1981) p. 19.

[35] Alexei Pankin Douglas McCune, Robert Andre, Glenn Bateman, and Arnold Kritz, Computer Phys. Communications **159**, 157 (2004).

[36] R. Guirlet, C. Giroud, T. Parisot, M. E. Puiatti, C. Bourdelle, L. Carraro, N. Dubuit, X. Garbet, and P. R. Thomas, Plasma Phys. Controlled Fusion **48**, B63 (2006).

[37] C. Angioni, E. Fable, M. Greenwald, M. Maslov, A. G. Peeters, H. Takenaga, and H. Weisen, Plasma Phys. Controlled Fusion **51**, 124017 (2009).

[38] K. Berhinger, JET Joint Undertaking Report JET-R(87)08, Abingdon, United Kingdom (1987).

[39] R. Dux, Max Planck Institüt für Plasmaphysik Report jpp 9/82, Garching, Germany (2007).

[40] C. B. Markwardt, Astronomical Society of the Pacific Conference Series, Vol. 411, D. A. Bohlender, D. Durand, P. Dowler (eds), pp. 251-254 (2009).

[41] N. T. Howard, M. Greenwald, D. R. Mikkelsen M. L. Reinke, A. E. White, D. Ernst, Y. Podpaly, and J. Candy, Nucl. Fusion **52**, 063002 (2012).

[42] R. Dux, R. Neu, A. G. Peeters, G. Pereverzev, A. Mück, F. Ryter, J. Stober, and ASDEX Upgrade Team, Plasma Phys. Controlled Fusion **45**, 1815 (2003).

[43] M. R. Wade, W. A. Houlberg, and L. R. Baylor, Phys. Rev. Lett. **45**, 1815 (2003).

[44] C. Angioni, P. Mantica, T. Pütterich, M. Valisa, M. Baruzzo, E. A. Belli, P. Belo, F. J. Casson, C. Challis, P. Drewelow, C. Giroud, N. Hawkes, T. C. Hender, J. Hobirk, T. Koskela, L. Lauro Taroni, C. F. Maggi, J. Mlynar, T. Odstrcil, M. L. Reinke, M. Romanelli, and JET EFDA Contributors, Nucl. Fusion **54**, 083028 (2014).

[45] T. Pütterich, R. Dux, R. Neu, M. Bernert, M. N. A. Beurskens, V. Bobkov, S. Brezinsek, C. Challis, J. W. Coenen, I. Coffey, A. Czarnecka, C. Giroud, P. Jacquet, E. Joffrin, A. Kallenbach, M. Lehnen, E. Lerche, E. de la Luna, S. Marsen, G. Matthews, M.-L. Mayoral, R. M. McDermott, A. Meigs, J. Mlynar, M. Sertoli, G. van Rooij, the ASDEX Upgrade Team and JET EFDA Contributors, Plasma Phys. Controlled Fusion **55**, 124036 (2013).

FIG. 1: (Color online) Influx of carbon after ELM suppression. (a) Plasma line-averaged density and I-coil current, (b) D_α emission indicating ELM-suppression period and (c) Z_{eff} at $\rho \approx 0.75$ determined from charge-exchange recombination spectroscopy.

FIG. 2: (Color online) Impurity confinement in L-mode (black), ELMing H-mode (red), and standard ELM-free H-mode (green) plasmas. (a) Plasma line-averaged density and D_α, (b) UV emission from helium-like chlorine, (c) UV nickel emission and (d) ratio of radiated power to auxiliary heating power. Particle confinement time in (b) is $\tau_p \approx 100$ for L-mode and 480 ms in ELMing H-mode. $\tau_p/\tau_e \approx 1.3$ in L-mode and 4.0 for ELMing H-mode. Impurity confinement is effectively infinite in the ELM-free H-mode.

FIG. 3: (Color online) (a) Fluorine emission decay and exponential fit, (b) D_α and ELM frequency. Impurity confinement time in the presence of 40 Hz ELMs is approximately 335 ms. With higher ELM frequency the impurity is removed more rapidly.

FIG. 4: (Color online) (a) Plasma line-averaged density, I-coil current and D_α indicating ELM suppression. (b) Fluorine emission decay and exponential fit. Impurity confinement time during RMP ELM-suppression is $\tau_p \approx 317$ ms.

FIG. 5: (Color online) (a) Plasma line-averaged density and D_α indicating no ELMs. (b) Magnetic spectrogram displaying coherent fluctuations, and (c) fluorine emission decay and exponential fit. Impurity confinement time during coherent EHO is $\tau_p \approx 327$ ms.

FIG. 6: (Color online) (a) Plasma line-averaged density and D_α indicating no ELMs. (b) Magnetic spectrogram displaying broadband fluctuations, and (c) fluorine emission decay and exponential fit. Impurity confinement time during broadband EHO is $\tau_p \approx 405$ ms.

FIG. 7: (Color online) BES fluctuation intensity for broadband and coherent EHO.

FIG. 8: (Color online) Plasma profiles in ELMing (156823,black), RMP ELM-suppressed (154858,red) and QH-mode conditions (153298,green) as a function of normalized toroidal flux, ρ_N. Toroidal rotation (Ω) for QH-mode in (d) is opposite to the direction of the plasma current.

FIG. 9: (Color online) TGLF linear growth rates for (a) ELMing, (b) RMP ELM-suppressed and (c) QH-mode discharges seen in Fig. 8 as a function of normalized toroidal flux, ρ_N.

FIG. 10: (Color online) Experimental profiles and TGYRO flux-matched profiles of (a) electron density, (b) electron temperature and (c) ion temperature for ELMing plasma seen in Fig. 8.

FIG. 11: (Color online) Experimental profiles and TGYRO flux-matched profiles of (a) electron density, (b) electron temperature and (c) ion temperature for RMP ELM-suppressed plasma seen in Fig. 8.

FIG. 12: (Color online) Experimental profiles and TGYRO flux-matched profiles of (a) electron density, (b) electron temperature and (c) ion temperature for QH-mode plasma seen in Fig. 8.

FIG. 13: (Color online) STRAHL simulation of fluorine time history in ELMing plasma 156823 for extracting transport coefficients with experimental measurements displayed with error bars and STRAHL solution in red for outer through inner radii (a-f). Radial coordinates of normalized toroidal flux (ρ_N) and normalized poloidal flux (ψ_N) are included.

FIG. 14: (Color online) STRAHL simulation of fluorine time history in RMP ELM-suppressed plasma 154858 for extracting transport coefficients with experimental measurements displayed with error bars and STRAHL solution in red for outer through inner radii (a-g). Radial coordinates of normalized toroidal flux (ρ_N) and normalized poloidal flux (ψ_N) are included.

FIG. 15: (Color online) STRAHL simulation of fluorine time history in QH-mode plasma 153298 for extracting transport coefficients with experimental measurements displayed with error bars and STRAHL solution in red for outer through inner radii (a-g). Radial coordinates of normalized toroidal flux (ρ_N) and normalized poloidal flux (ψ_N) are included.

FIG. 16: (Color online) Transport coefficients determined from STRAHL modeling (grey band) for ELMing discharge 156823 displayed in Fig. 14, and coefficients from NEO and TGLF. (a) Fluorine diffusion coefficient, (b) convective velocity and (c) peaking factor.

FIG. 17: (Color online) Transport coefficients determined from STRAHL modeling (grey band) for RMP ELM-suppressed discharge 154858 displayed in Fig. 14, and coefficients from NEO and TGLF. (a) Fluorine diffusion coefficient, (b) convective velocity and (c) peaking factor.

FIG. 18: (Color online) Transport coefficients determined from STRAHL modeling (grey band) for QH-mode discharge seen in Fig. 8, and coefficients from NEO and TGLF. (a) Fluorine diffusion coefficient, (b) convective velocity and (c) peaking factor.

FIG. 19: (Color online) STRAHL simulation of fluorine using NEO+TGLF transport coefficients displayed in Fig. 17, with experimental measurements displayed with error bars and STRAHL simulation in red for outer through inner radii (a-g).

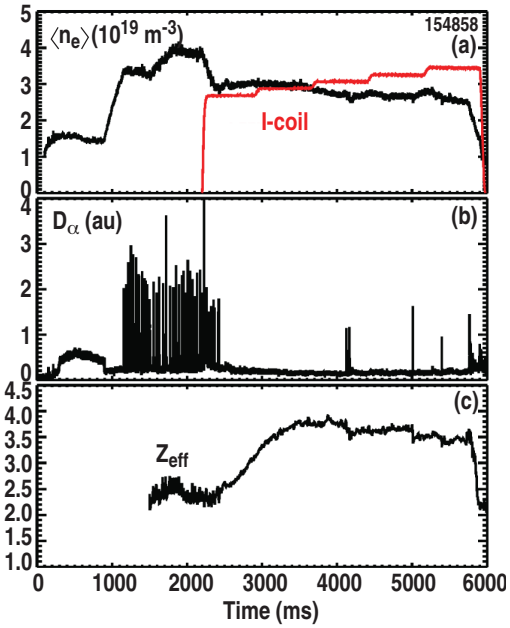

B.A. Grierson Figure 1

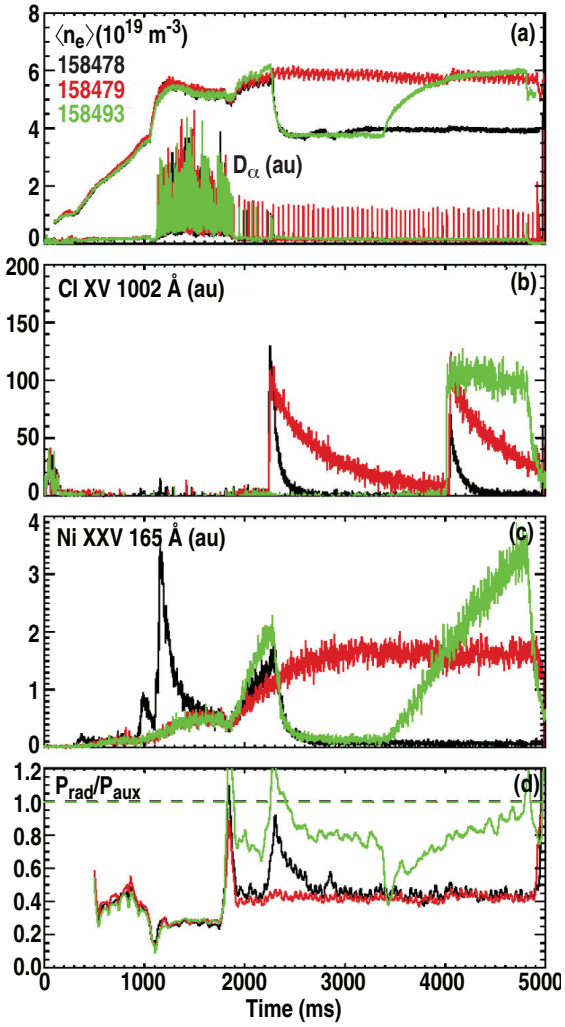

B.A. Grierson Figure 2

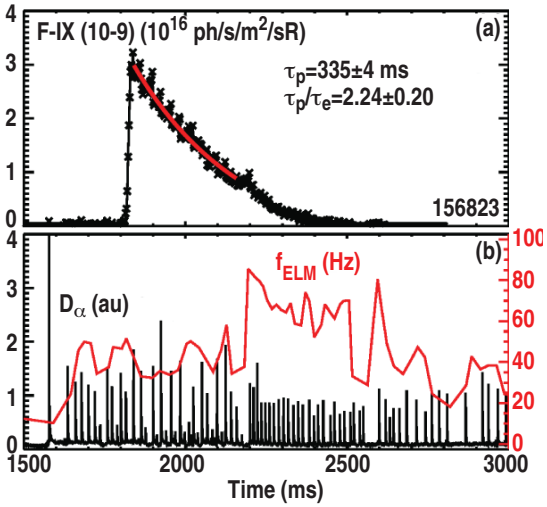

B.A. Grierson Figure 3

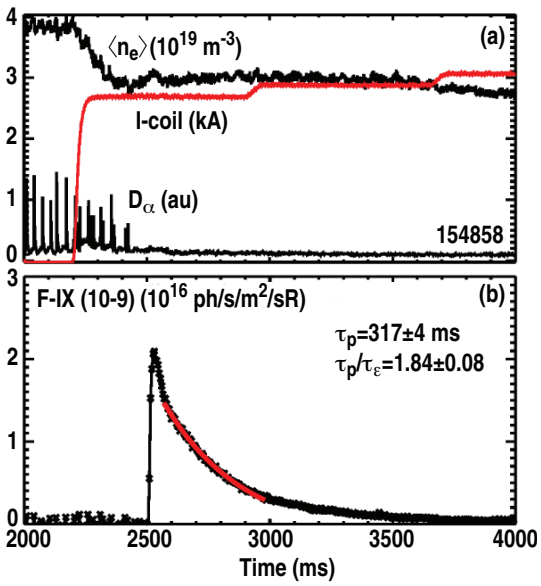

B.A. Grierson Figure 4

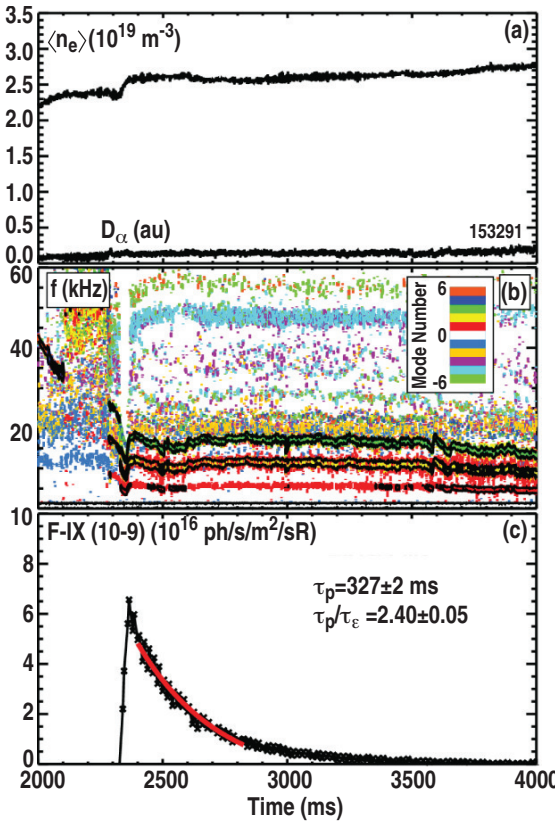

B.A. Grierson Figure 5

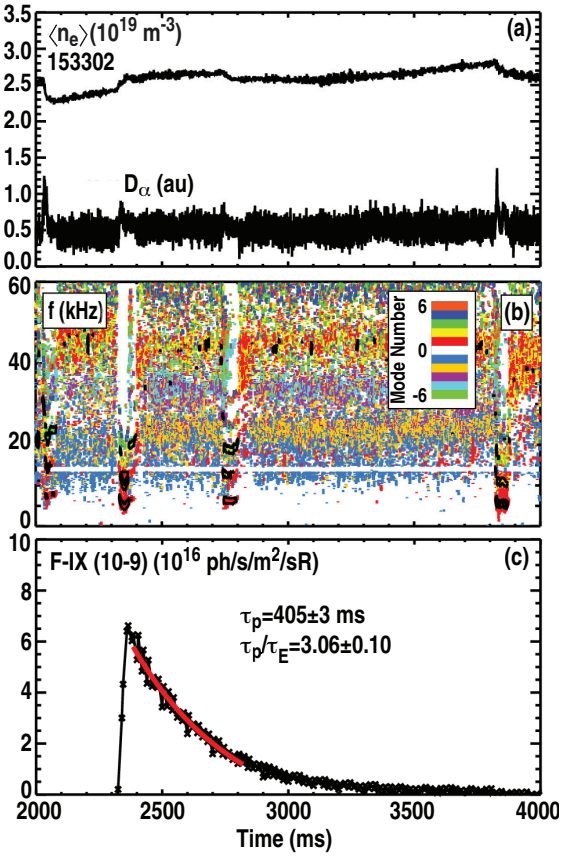

B.A. Grierson Figure 6

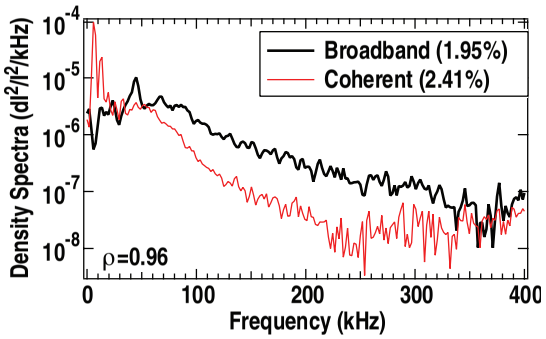

B.A. Grierson Figure 7

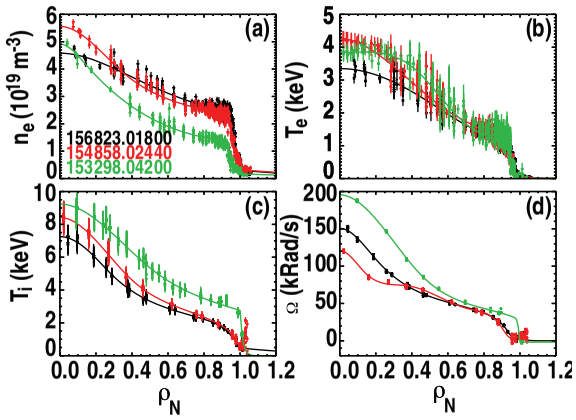

B.A. Grierson Figure 8

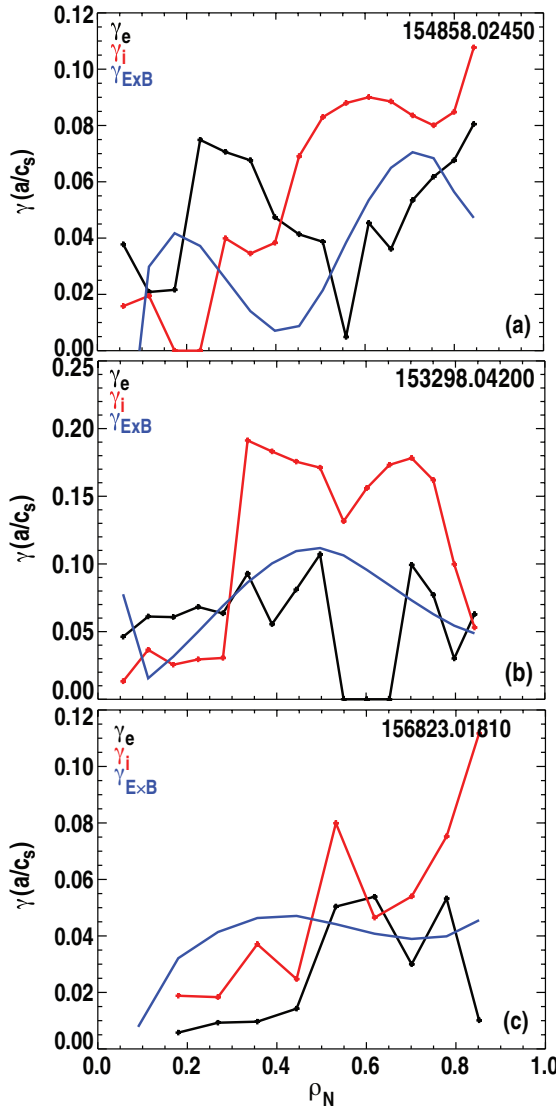

B.A. Grierson Figure 9

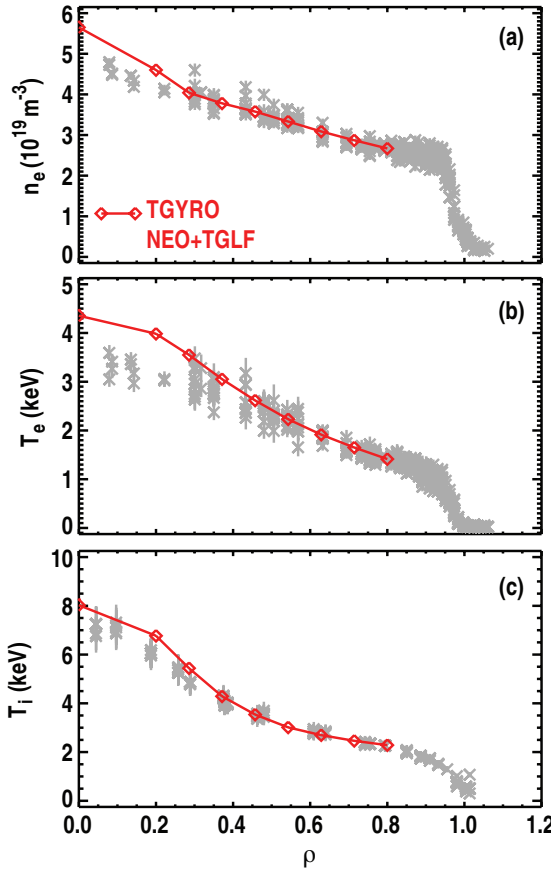

B.A. Grierson Figure 10

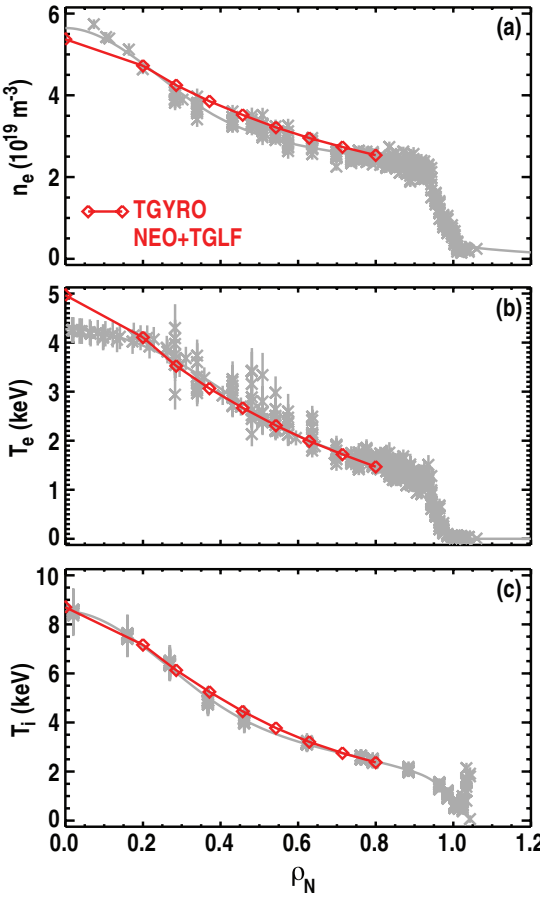

B.A. Grierson Figure 11

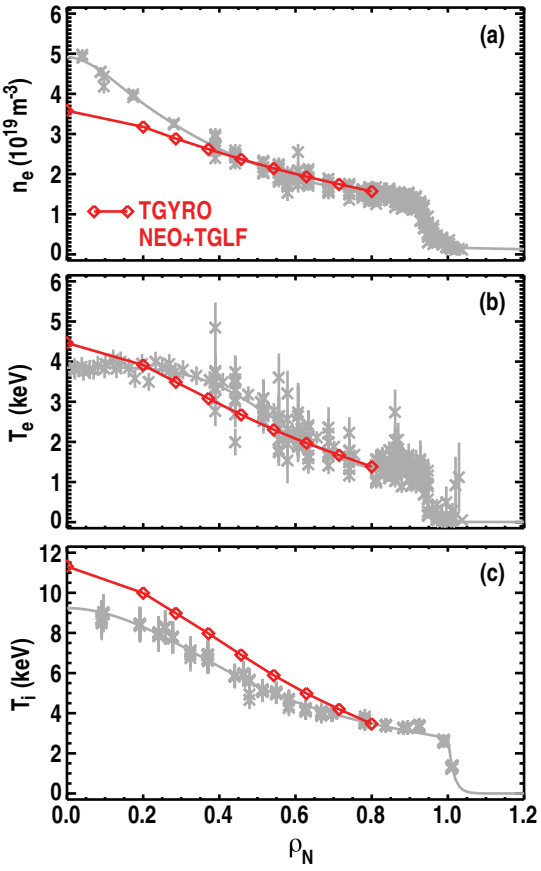

B.A. Grierson Figure 12

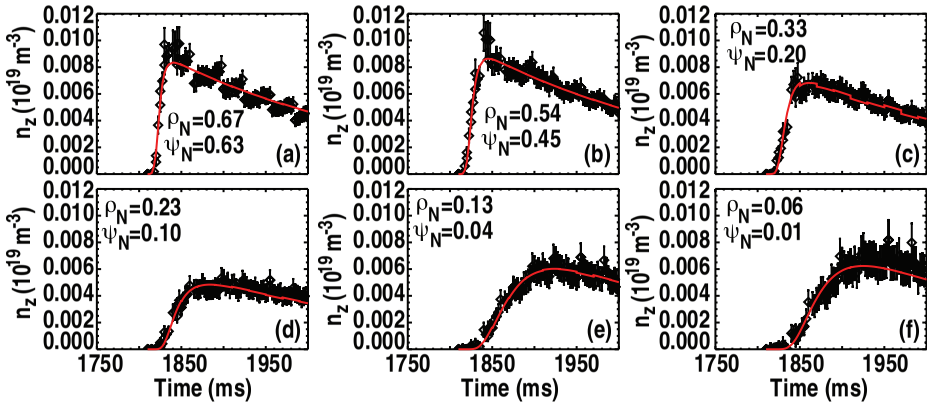

B.A. Grierson Figure 13

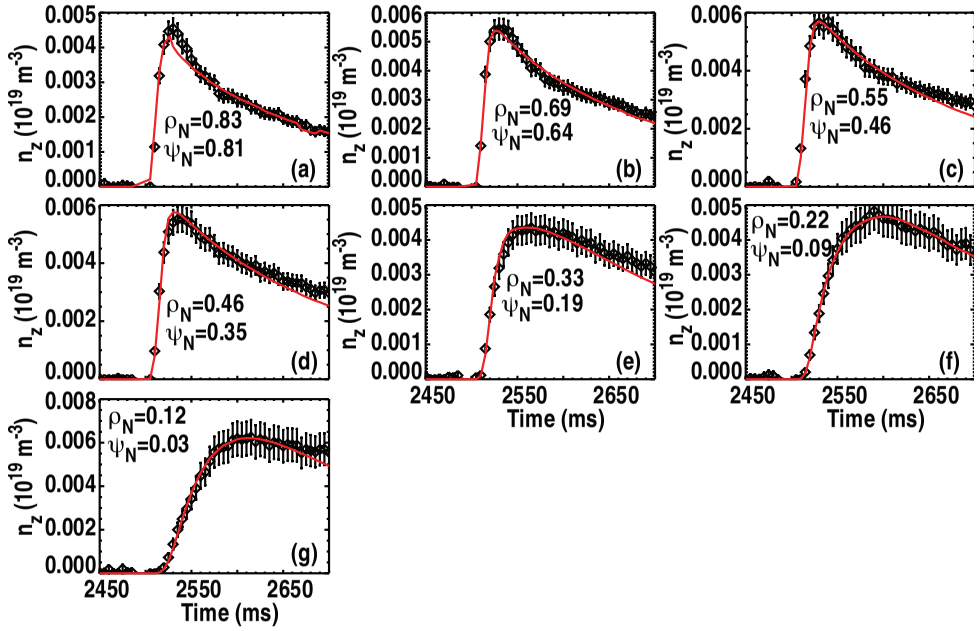

B.A. Grierson Figure 14

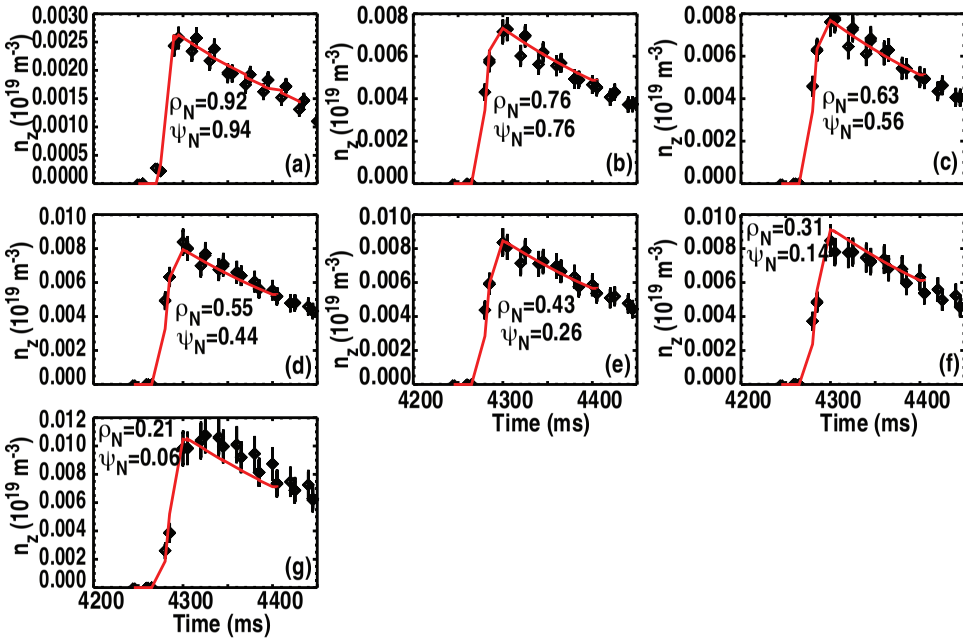

B.A. Grierson Figure 15

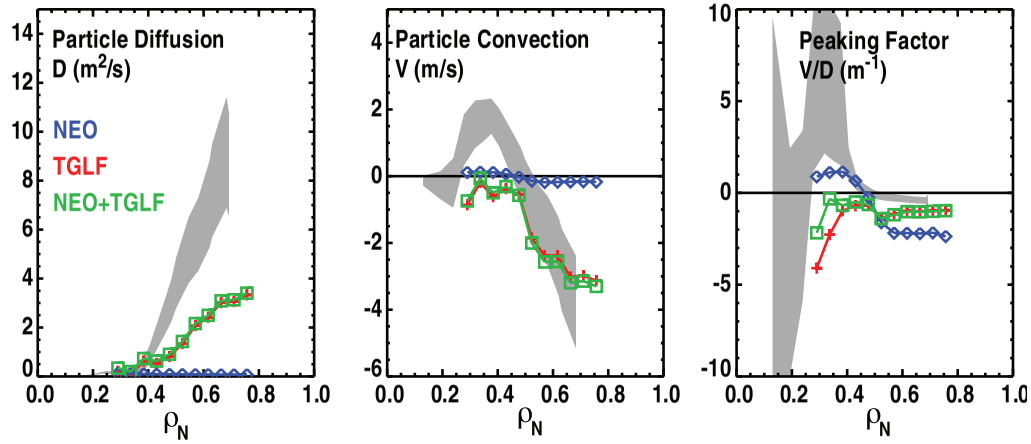

B.A. Grierson Figure 16

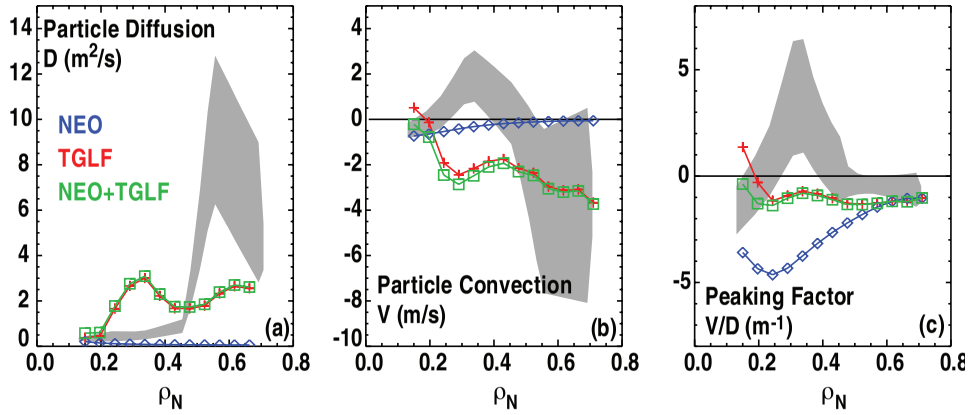

B.A. Grierson Figure 17

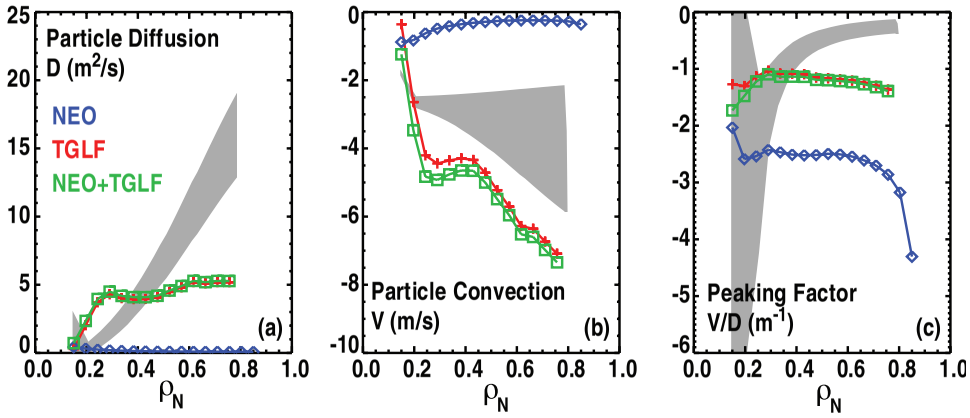

B.A. Grierson Figure 18

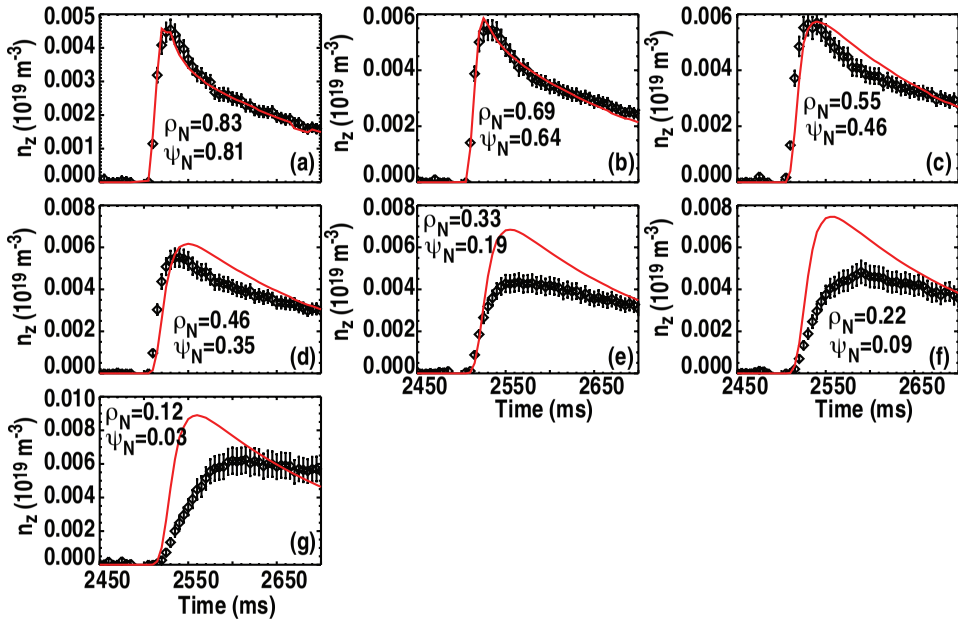

B.A. Grierson Figure 19